

Dewetted Au nanoparticles on TiO₂ surfaces –

Evidence of a size-independent plasmonic photo-electrochemical response

Markus Licklederer,^a Nhat Truong Nguyen,^a Reza Mohammadi,^b Hyoungwon Park,^c
Seyedsina Hejazi,^a Marcus Halik,^c Nicolas Vogel,^b Marco Altomare,^{a*} Patrik Schmuki^{a,d*}

^a Department of Materials Science and Engineering, Institute for Surface Science and Corrosion WW4-LKO, University of Erlangen-Nuremberg, Martensstrasse 7, D-91058 Erlangen, Germany.

^b Department of Chemical and Biological Engineering, Institute of Particle Technology, University of Erlangen-Nuremberg, Cauerstrasse 4, D-91058 Erlangen, Germany.

^c Department of Material Science and Engineering, Institute of Polymer Materials, University of Erlangen-Nuremberg, Martensstrasse 7, D-91058 Erlangen, Germany.

^d Chemistry Department, Faculty of Sciences, King Abdul-Aziz University, 80203 Jeddah, Saudi Arabia

* Corresponding authors. Email: marco.altomare@fau.de
schmuki@ww.uni-erlangen.de

link to the published article:

<https://pubs.acs.org/doi/abs/10.1021/acs.jpcc.9b02769>

Abstract

Flat TiO₂ layers are deposited by magnetron sputtering on Ti/Si wafers. The TiO₂ surfaces are then sputter-coated with thin Au films of a nominal thickness of 0.5-10 nm that are converted by solid-state dewetting into Au nanoparticles of tuneable size and spacing; the Au nanoparticle size can be tuned over a broad range, i.e. ca. 3-200 nm. The Au-decorated TiO₂ surfaces enable plasmonic photo-electrochemical water splitting under visible light illumination (450-750 nm). The water splitting performance reaches a maximum for TiO₂ layers decorated with ~ 30 nm-sized Au particles. As expected, optical absorption measurements show a red shift of the plasmonic extinction band with increasing the Au nanoparticle size. However, the plasmonic photocurrent is found to peak at ~ 600 nm regardless of the size of the Au nanoparticles, i.e. the plasmonic photocurrent band position is size-independent. Such a remarkable observation can be ascribed to a hot electron injection cut-off effect.

Keywords: dewetting; Au nanoparticle; TiO₂; plasmon resonance; solar water splitting

1. Introduction

One of the most investigated metal oxide semiconductor materials for photocatalytic and photoelectrochemical generation of hydrogen is titanium dioxide (TiO_2). The reasons are, on the one hand, its outstanding chemical stability, nontoxicity, low cost and large availability, and, on the other hand, its semiconductive properties and electronic structure, i.e. the position of TiO_2 valence and conduction bands (VB and CB) is suitable to enable water splitting into O_2 and H_2 gas.¹

Large efforts have been given in the last decades to study the photocatalytic and photoelectrochemical performance of TiO_2 , particularly in various nanostructured forms.^{1,2} Nevertheless, regardless of its morphology, a major drawback limiting the efficiency of TiO_2 is its “wide” band gap, i.e. of 2.8-3.2 eV depending on the crystallographic phase (i.e. anatase or rutile). The “wide” band gap sets a limit to TiO_2 light absorption to only UV photons, i.e. only ~ 5 % of the solar spectrum.³

Band gap engineering to enable visible light absorption of TiO_2 , with e.g. non-metal elements (N-doping) has been widely explored,⁴ as well as TiO_2 surface modification (e.g. sensitization) with dye molecules or quantum dots.^{5,6,7}

Intense research activity has also focused on the possibility to combine TiO_2 with plasmonic metal (Au or Ag, Al) nanoparticles (NPs).⁸⁻¹¹ The plasmonic light absorption of metal nanostructures can potentially cover a broad visible light range upon a suitable tuning of the metal NP features (e.g. size, shape, aspect ratio, dielectric constant of the surrounding, among other parameters).^{9,12-14} An advantage of using gold as the plasmonic material is its (photo)stability.^{9,12-14}

Plasmon resonance can be described as the collective oscillation of the free charge in a conducting material.¹⁵ For metal nanoparticles (NP),¹⁰ localized surface plasmon resonance (LSPR) is stimulated by absorption of light of a suitable wavelength range. When placed on a

semiconductor, plasmonic NPs can generate charge carriers, e.g. hot electrons, which can consequently be injected into the semiconductor substrate.^{9,12-14} “Hot” charge carriers, generated upon visible light illumination of Au NPs supported on a TiO₂ photo-anode, can be used in a photo-electrochemical configuration for water splitting. For example, Au hot electrons can be injected into the semiconductor and contribute to the generated photocurrent (evolving H₂ gas at the Pt counter electrode), while hot holes are able to drive oxidation reactions at the Au nanoparticle surface.¹⁶ In other words Au and TiO₂ can in principle act in tandem as complementary light absorbers, where TiO₂ and Au NPs harvest UV ($\lambda < 400$ nm) and visible ($400 \text{ nm} < \lambda < 800$ nm) light, respectively.

Plasmon-induced photo-electrochemical activity has been observed for different types of Au-TiO₂ photo-electrodes, where TiO₂ can be in various geometries, e.g. ranging from a “planar architecture” such as compact or mesoporous (nanoparticulate) films, or in the form of arrays of one-dimensional (1D) nanostructures e.g. nanotubes, nanowires and nanorods. Plasmonic Au nanoparticles can, in a simplest approach, be formed by wet chemical synthesis from Au precursors, using reducing chemical agents, or by photo-deposition.^{9,11,16-21}

In the present work we produce Au nanoparticles by solid state dewetting of thin Au films deposited by Ar plasma sputtering on flat TiO₂ layers. The TiO₂ layers are fabricated by reactive magnetron sputtering of Ti in an Ar-O₂ plasma, and feature a surface roughness < 1 nm. The flat and smooth surface of the TiO₂ substrates allows for dewetting of Au films to occur in an ordered fashion, thus forming defined Au particles of tunable size and distribution; Au nanoparticle size and spacing can be finely controlled by the initial thickness of the Au films. We find that Au nanoparticle dewetted at TiO₂ rutile surfaces enable solar photo-electrochemical water splitting, and enable the generation of plasmonic photocurrent in the 450-750 nm range. The photocurrent is maximized when the dewetted Au nanoparticles are ~ 30 nm-sized.

Interestingly, while optical absorption measurements show a red shift of the plasmonic extinction band with increasing the Au NP size, we observe that the plasmonic photocurrent peaks at ~ 600 nm regardless of the Au particle size. Such a discrepancy between the optical absorbance and the photo-electrochemical features can be ascribed to a hot electron injection cut off effect, namely due to different size-dependent plasmon decay mechanisms.

2. Experimental Section

The TiO₂ surfaces were produced by magnetron sputtering in an ultra-high vacuum (UHV) chamber (Createc, SP-P-US-6M-3Z) on Ti metal-coated Si wafer (3 inch, Microchemicals, Si (100) p-type). Control experiments were carried out by producing the TiO₂ surfaces also on other Ti-coated substrates, such as 3 inch SiO₂/Si wafer (Microchemicals, Si (100) p-type + 100nm SiO₂) and quartz glass slides (GBV, Germany).

The titanium metal coating was sputtered (e.g. onto the Si substrate) from a Ti target (Hauner HMW, 99.999 %) operated in direct current (DC) mode, with a deposition power of 150 W, at room temperature. During deposition, the working pressure was held constant at 1×10^{-3} mbar and the Ti metal deposition time was 10 min, forming a Ti metal film with a thickness of 75 nm. Afterwards the Ti metal-coated Si substrates were patterned with a frame mask, leaving behind free (unmasked) Ti patches with a size of 1.4×2.4 cm². The unmasked Ti surface was then coated with amorphous 75 nm-thick TiO₂ layers deposited by reactive magnetron sputtering, with a deposition power of 150 W, at room temperature, in an Ar-O₂ plasma (Ar-O₂ ratio 1:5). During deposition, the working pressure was held constant at 1×10^{-3} mbar. The deposition time was 60 min, forming a TiO₂ film with a thickness of 75 nm.

The TiO₂ surfaces formed on Ti/Si substrates were then cut into 2.5×3.0 cm² samples, having a Ti-coated frame (surrounding the TiO₂-coated patch) that served as back-side electric contact (electron collector scaffold) in the photo-electrochemical measurements.

The samples were then coated with Au films of different thicknesses (0.5-10 nm) using a plasma sputtering device (EM SCD500, Leica). The amount of Au, in terms of nominal Au film thickness, was controlled by an automated quartz crystal microbalance (thickness monitor).

The Au-coated TiO₂ substrates were then annealed in a tubular furnace at 450°C in air for 1h. This thermal treatment is key as it simultaneously leads to (i) crystallization of the amorphous TiO₂ surface into rutile phase, and (ii) solid-state dewetting of the Au films into Au nanoparticles of controllable size and spacing.

For the optical measurements (experimental described below), Au NPs were formed by argon plasma deposition of Au films of different thicknesses (0.5-10 nm) on quartz glass slides (1.5 x 1.5 cm², GVB, Germany). The quartz substrates were previously cleaned by sonication in acetone, ethanol and deionized water (15 min for each step), and then dried in a N₂ stream. After the deposition, the quartz supported Au films were dewetted in a tubular furnace at 450°C in air (1 h).

The morphology of the Au-decorated rutile TiO₂ surfaces was characterized using a field emission scanning electron microscope (Hitachi FE-SEM, 4800). The chemical composition of the samples was carried out by X-ray photoelectron spectroscopy (XPS, PHI 5600, US). XPS spectra were acquired using Al X-ray source. The XPS spectra were corrected in relation to the C 1s signal at 284.6 eV. PHI MultiPak™ software and database were used for quantitative analysis. X-ray diffraction (XRD) with an X'pert Philips MPD (equipped with a Panalytical X'celerator detector) was used to examine the crystallographic properties of the materials. Depth profiling was carried out using the instrument's Ar⁺ sputter source operated at 3 kV, 15 nA, rastered over a 3 × 3 mm² area with a sputtering angle of 45° to the surface normal. 1 min long sputter steps were repeated to analyze in depth the composition of the whole architectures until reaching the Si substrate. The atomic composition was determined between consecutive sputtering intervals, by evaluation the photoelectron peak areas, using the MultiPak™ processing software.

AFM imaging was performed using a Veeco Dimension 3100 Microscope, operated in tapping mode. Bruker silicon probes with a spring constant of 2 N m^{-1} and 70 kHz resonance frequency were used. The resolution was set to 1024×1024 pixels for measured surface of 2×2 or $10 \times 10 \mu\text{m}^2$. Processed data were acquired with Gwyddion 2.42. The RMS roughness values were evaluated by the statistical quantities tool embedded in the Gwyddion SPM analysis software. The lower threshold was set to 0.05 nm to correct for sample roughness.

The IPCE spectra were recorded with a setup comprising an Oriel 6356 150 W Xe arc lamp as light source and an Oriel cornerstone 7400 1/8 monochromator. The measurements were carried out in aqueous 0.1 M Na_2SO_4 solutions at an applied potential of 0.5 V in an electrochemical cell equipped with a quartz glass window and operated in a three electrode configuration with the Au-TiO₂ structures used as working electrode, a Ag/AgCl electrode as reference and a Pt foil as counter electrode. Photo-current transients under monochromatic light illumination (600 nm) were also recorded under constant external applied bias (+500 mV) and 20s-10s light on-off cycles.

The photo-electrochemical water-splitting performance of the samples was investigated in aqueous 1 M KOH solutions with a three-electrode configuration: the Au-TiO₂ structures were used as working electrode, a saturated Ag/AgCl electrode was used as the reference and a platinum foil was used as the counter electrode. For the photo-electrochemical linear sweep voltammetry (LSV) experiments, an external potential was applied to the photoelectrochemical cell provided by a scanning potentiostat (Jaissle IMP 88 PC), and was swept from -0.65 V to +1.25 V. The experiments were carried out under simulated AM 1.5 illumination provided by a solar simulator (300 W Xe with a Solarlight optical filter). The light intensity emitted by the solar simulator (operated without the cut off filter) was measured prior to the experiments using a calibrated Si photodiode and the distance between the light source and the photo-anode was adjusted to illuminate the samples with an irradiation power of 100 mW cm^2 . Photo-current transients under visible light illumination (solar simulator with 420 nm cut-off filter) and under

illumination with a 520 nm laser (1 W, OdiForce Lasers, OFC 420-G1000) were also recorded under a constant applied bias (+500 mV) and under 30s-10s light on-off cycles.

To study the optical properties of the quartz supported Au nanoparticles, we used a UV-Vis-IR spectrometer (Perkin-Elmer Lambda950) with an integrating sphere and illumination beam of approximately 8 mm in diameter. We performed the transmission measurements from 300 to 1500 nm with 2 nm resolution.

3. Results and Discussion

3.1 Physicochemical characterization

The structure of the plasmonic Au-TiO₂ surfaces produced in this work is outlined in Fig. 1a. The TiO₂ surfaces are produced on Ti-coated Si wafer substrates by magnetron sputtering. The SEM analysis of a cross-sectional cut of a typical structure is shown in Fig. 1b, where one can see (from bottom to top) the Si/Ti and Ti/TiO₂ interfaces (highlighted with dotted lines). The TiO₂ and Ti layers both have a thickness of 75 nm.

The XRD data in Fig. 1c reveal that in the as-deposited architecture, the TiO₂ surface is amorphous; no reflections of crystalline TiO₂ polymorphs can be seen. However, a thermal treatment in air at 450°C (1 h) leads to crystallization into rutile phase. This is evident from the appearance of a peak at 27.5° upon annealing, which can be attributed to the TiO₂ rutile (110) reflection.²² Additional XRD data (measured in the 20-80° 2θ range) confirm the formation of TiO₂ rutile phase – provided in Fig. S1a. The XRD data in Fig. S1b were collected by θ-2θ rocking curve scans. Aside from the Si peak at 70° (ascribed to the single crystal Si substrate) one can notice that even upon annealing the Ti bottom layer remains in the metallic state; this is proved by the presence of a Ti reflection at 38°.

The crystalline TiO₂ surfaces were characterized by XPS in view of their chemical composition. The XPS survey in Fig. S1c shows the layers to be composed of Ti and O (and adventitious C).

We found a surface 1:2 Ti:O compositional ratio (Ti ~ 33% and O ~ 67%), which is in line with the TiO₂ stoichiometry. The high resolution spectra in the Ti 2p and O 1s regions (Fig. S1d,e) show peaks that fit well to TiO₂ XPS data reported in the literature.²³ Such Ti 2p and O 1s peaks seem not to vary significantly upon annealing and conversion of the amorphous TiO₂ into crystalline rutile phase.

The XPS sputter profile of a typical TiO₂/Ti layer is presented in Fig. 1d (both before and after TiO₂ crystallization). In both cases, one can identify two interfaces, i.e. the TiO₂/Ti and Ti/Si interfaces (from top to bottom), at a depth of approximately 75 and 150 nm, respectively.

The surface roughness of as-deposited and crystallized TiO₂ surfaces was investigated by AFM measurements (Fig. 1e and Fig. 1f, respectively). As-deposited TiO₂ surfaces show a RMS surface roughness < 1 nm (precisely, 9.6 Å). Upon annealing, the TiO₂ surface roughness is found to increase to 4.5 nm; this is ascribed to TiO₂ crystallization into rutile phase, and consequent grain growth and faceting. However, the crystalline TiO₂ surfaces remain homogeneous and conformally-coated on the Ti/Si substrates, and no through-layer pinholes could be observed.

The Au nanoparticles are formed on the TiO₂ surfaces by solid-state “dewetting” of sputtered Au films.^{24,25} Firstly, Au thin films with a nominal thickness in the 0.5-10 nm range are deposited on the amorphous TiO₂ surfaces. The Au films were then converted into self-ordered Au particles by thermal dewetting. Dewetting occurs as thin metal films are unstable in the as-deposited state and when heated up to a certain temperature, tend to split-open and agglomerate, forming metal particles via surface diffusion.²⁶ In our recent work, we explored metal dewetting phenomena at the surface of semiconductor metal oxides, e.g. TiO₂, to fabricate photocatalysts and photo-electrodes.²⁶⁻²⁹

In the present work, the Au-films deposited at the TiO₂ surfaces were dewetted by a thermal treatment in air at 450°C (1 h); this is well in line with the melting point of Au ($T_{m,Au} = 1064^\circ\text{C}$), as depending on the metal film thickness, solid state dewetting is expected to occur at

temperatures well below the metal melting point, e.g. between 1/3 and 1/2 of $T_{m,Au}$.^{24,25} Dewetting occurs (vide supra) together with the crystallization of the amorphous oxide surface into rutile TiO₂ phase.

The pristine and Au-decorated TiO₂ surfaces were analyzed by SEM. The results are compiled in Fig. 2 (additional SEM data are in Fig. S2). The SEM images in Fig. 2b-g (and Fig. S2) demonstrate that the size (and spacing) of the dewetted Au NPs can be well controlled over a broad range (from ca. 3 to 200 nm). The data in Fig. S3a show the size distribution statistics of Au NPs dewetted from Au films of different initial nominal thicknesses. Table S1 and Fig. S3b summarize the results. We observe, in line with previous work, that the thicker the Au film, the larger the Au NP size and spacing, and the broader their size distribution statistics.^{24,25} For example, dewetting of a 0.5 nm-thick Au film forms 3.2 nm-sized Au NPs; a 2 nm-thick Au film forms instead 32 nm-sized Au particles (i.e. one order of magnitude bigger NPs). Also, it seems that within the size range explored in this work, the Au NP size scales linearly with the Au film initial thickness (Fig. S3b).

3.2 Photo-electrochemical characterization

The pristine and Au-decorated TiO₂ surfaces were investigated as photo-anodes for solar photo-electrochemical water splitting. The photo-electrochemical results are compiled in Fig. 3. Fig. 3a shows the IPCE spectra of pristine and TiO₂ surfaces decorated with dewetted Au NPs of different sizes. The Au-TiO₂ samples are labeled according to the initial nominal thickness of the sputtered Au film.

Pristine TiO₂ surfaces (sample “0 nm”) generate photocurrent only upon band gap excitation, i.e. under UV light illumination. Well in line with the rutile phase composition, the photocurrent onset is at ~ 410 nm, corresponding to a band gap energy of 3.0 eV (see band gap estimation in Fig. S4).³⁰ On contrary, all the Au-decorated TiO₂ surfaces generate photocurrent not only upon

TiO₂ band gap excitation, but also under visible light illumination, showing an evident photocurrent peak in the 450-750 nm range (inset in Fig. 3a).

In the following sections we examine and discuss the different contributions to the photocurrent, i.e. ascribed to TiO₂ UV light absorbance or Au plasmon resonance, in relation to parameters such as Au NP size, free TiO₂ surface, shading effects, hot carrier generation and extraction efficiency, and electron trapping effects.

3.3 UV light-induced photocurrent

In the UV region, the highest IPCE values are recorded for the pristine TiO₂ rutile surfaces (0 nm), which deliver a maximum IPCE of 20 % measured at 300 nm. Overall, the photocurrent trend at 300 nm is 0 nm > 2 nm > 5 nm > 3 nm > 10 nm > 1 nm >> 0.5 nm. To interpret these results one may take into account that the photocurrent generation under UV light illumination may be affected by factors such as (i) light shading effects ascribed to the Au NPs decorated at the TiO₂ surface – this effect is expected to set in mainly for large Au particles (e.g. > 50 nm); and (ii) the extent of free (uncoated) TiO₂ surface. The former factor (Au NP size and surface coverage) can influence the photon flux reaching the TiO₂ surface. The latter is connected to the efficiency of TiO₂ hole injection into the electrolyte; it is reasonable to assume that the ease of hole transfer to the electrolyte increases with increasing the free (uncoated) TiO₂ surface, while hole transfer becomes gradually more hampered with increasing the Au surface coverage (the consequent hole accumulation in TiO₂ can result in charge recombination and thus in a limited photocurrent). When plotting the free TiO₂ surfaces and the IPCE (measured at 300 nm) as a function of the Au film initial thickness (Fig S5), no straightforward correlation between these parameters can be found.

Hence, we propose that the photocurrent measured under UV light illumination may be also affected by the ability of Au NPs to trap TiO₂ conduction band electrons. In a PEC configuration under the sole UV light illumination, the photocurrent can only be caused by photo-promoted

electrons in TiO₂ (band gap excitation). These electrons have to diffuse through the TiO₂ rutile layer to be collected by the (Ti metal) back contact. In spite of the applied anodic bias (that causes upward band bending in TiO₂ and thus generate an electron-depleted space charge region in the semiconductor) it may however occur that photo-promoted electrons (more likely those generated at the surface or sub-surface of the TiO₂ photo-anode) can be trapped by Au NPs. In previous work, the deposition of noble metal NPs on the surface of TiO₂ photo-anodes was observed to lead to an evident UV photocurrent drop,^{31–33} although such nanoparticles had an average size < 10 nm and were thus not expected to contribute to UV light shading effects. Interestingly, Fig. S6 shows the trend of the Au NP surface decoration density and IPCE (measured at 300 nm) as a function of the Au film initial thickness. The lowest IPCE values are measured for the highest Au NP decoration density (which are obtained by dewetting 0.5 nm and 1 nm-thick Au layers). These results seem to point to a trapping effect for UV light-generated TiO₂ CB electrons that becomes dominant for high surface decoration densities of Au-TiO₂ Schottky junctions, i.e. the higher the decoration density (number of Au NPs per unit area), the larger the electron trapping effect and, consequently, the lower the UV photocurrent.

3.4 Plasmonic photocurrent

The photocurrent observed in the visible light region (inset in Fig. 3a) can be ascribed to surface plasmon resonance (SPR) effects enabled by the Au NPs dewetted at the TiO₂ surfaces. Please note that no visible light photocurrent can be observed for pristine TiO₂ surfaces. The photocurrent results are summarized in Fig. 3b as a function of the Au film initial thickness. Fig. 3c illustrates the photocurrent transients measured for the different photo-anodes under monochromatic visible light (600 nm) illumination. From Fig. 3b one can see that the photocurrent response increases with increasing the Au film thickness from 0.5 nm to 2 nm. A further increase of the Au film thickness is found detrimental as it leads to a remarkable photocurrent drop. A Au film with an initial thickness of 2 nm, which forms by dewetting ~ 30

nm-sized Au NPs at the TiO₂ surface, leads to the highest plasmonic photocurrent response, corresponding to an IPCE of 0.4 % (inset in Fig. 3a).

Previous work on plasmonic metal nanoparticles on a semiconductor surface demonstrated that the LSPR effect, in terms of visible light absorption cross section, hot carrier generation efficiency and intensity of the plasmon-induced electromagnetic field, is dependent on the metal particle size and spacing.⁹ For Au NPs on TiO₂, the absorption band associated to plasmon resonance falls at a specific wavelength in the 500-600 nm range as a function of the Au NP shape and size.³⁴⁻³⁸ Our results, however, show that the plasmonic effect varies as a function of the Au NP size only in terms of photocurrent magnitude (photocurrent density), while the band position is found to be constant at ~ 600 nm regardless of the Au NP size.

To clarify this aspect, we measured the optical absorbance of Au NPs dewetted on quartz glass slides (data compiled in Fig. S7a,b). In average, the extinction maxima are observed in the 520-570 nm region, i.e. are blue shifted compared to the plasmonic photocurrent peaks; this is due to the refractive index of the substrate (quartz glass vs. TiO₂). In other words, the Au plasmon band measured by IPCE at longer wavelength ($\lambda_{\text{max}} \sim 600$ nm) is due to the higher refractivity index of TiO₂ compared to quartz.³⁹ More importantly, the optical measurements show a red shift of the plasmonic extinction band maxima ($\Delta\lambda = 14$ nm) with increasing the Au NP size (initial Au film thickness increasing from 0.5 nm to 5 nm); see data in Fig. S7c. The red shift is accompanied by an evident peak broadening. Particles dewetted from a 10 nm thick Au film show an even more pronounced red shift ($\Delta\lambda = 58$ nm) and a dramatic band widening effect (see the SI for more details).

Such a mismatch between the optical absorbance and PEC performance, and the size-independence of the plasmonic photocurrent peak, can be ascribed to a hot electron injection cut off effect. In a PEC configuration, plasmonic electrons can contribute to the photocurrent only if they are injected into the CB of the semiconductor substrate. Our optical measurements show that the larger the Au particles the longer the wavelength of maximum plasmonic

extinction. Interestingly, previous spectroscopic investigations demonstrated that plasmonic decay substantially varies in relation to the excitation wavelength, while it appears almost unaffected by the Au particle size.⁴⁰ More precisely, long-lived hot carriers were found to be generated by absorption of photons of relatively lower wavelength (e.g. $< \sim 560$ nm). On the contrary, hot electrons excited by longer wavelength were found to undergo rapid decay; in other words, bigger Au particles do absorb longer wavelength photons but the generated hot electrons recombine rapidly and thus cannot effectively contribute to the photocurrent; on the other hand, the relatively long lifetime of hot electrons excited with shorter wavelength photons allows for a more efficient charge extraction and injection into the TiO₂ surfaces. In our view, aside from a slower plasmon decay mechanism, hot electrons excited with shorter wavelength photons may be more efficiently injected into the semiconductor CB also owing to their higher energy level, which allows them to overcome the Schottky barrier at the Au/TiO₂ interface. In the case of our results, we can assume that such a hot electron injection energy cut off effect has a threshold wavelength at ~ 600 nm. At ~ 600 nm, hot electron excitation efficiently contributes to photocurrent. Below this wavelength the plasmonic extinction is limited (low optical absorption and hence small density of hot charge carriers), while above 600 nm the hot electrons may not possess sufficient energy to overcome the Schottky barrier. At the threshold wavelength (600 nm), the photocurrent is mainly determined by the Au NP size: a maximum charge separation and injection efficiency is observed for ~ 30 nm-sized Au NPs, as also reported in literature.^{41,42} In contrast, Au NPs < 10 nm only enable a relatively low light absorption, due to surface damping effects (e.g. Landau damping), while Au NPs > 40 nm typically lead to a less efficient hot electron injection into TiO₂ (it is in fact reported that the injection efficiency decreases with increasing the Au particle volume, keeping the particle aspect ratio constant).^{41,42}

For Au-TiO₂ structures formed from Au films with thickness in the 1-5 nm range, the photocurrent transients resemble a square wave signal, i.e. the response is characterized by an

instantaneous photocurrent increase up to a maximum photocurrent value upon light illumination, followed by a rapid photocurrent drop in the dark (Fig. 3c). In contrast, the response is relatively slow for sample 10 nm, and particularly sluggish (and “noisy”) for sample 0.5 nm; in line with what above, the origin of the sluggish photocurrent response for large Au NPs (dewetted from 10 nm thick Au film) can be a poor injection efficiency, while the reason for the sluggish and noisy response observed for sample 0.5 nm has yet to be clarified.

3.5 Solar photocurrent

The solar PEC water splitting ability of the photo-anodes was investigated by photo-electrochemical linear sweep voltammetry (LSV) experiments. Measurements were also performed by applying to an AM 1.5 light source (solar simulator) a 420 nm cutoff filter, in order to illuminate the photo-anodes with visible light only. The results (Fig. 3d) show that the I_{ph} onset is in any case at -500 mV. With the 420 nm cutoff filter, the Au NP-decorated TiO₂ surfaces generate photocurrent, while no photocurrent is observed for the reference pristine TiO₂.

The PEC results under full lamp illumination show that the water splitting ability of the Au-TiO₂ photo-anodes is higher than that of pristine counterparts; the Au plasmon resonance increases the photoresponse from 10.8 $\mu\text{A cm}^{-2}$ to 12.6 $\mu\text{A cm}^{-2}$ (at +500 mV vs. Ag/AgCl), which corresponds to a photocurrent increase of 16%. Please note that under the sole UV light illumination, the photocurrent of Au-TiO₂ structures was found to be lower than that of pristine TiO₂ layers (Fig. 3a). Therefore, one can conclude that under full lamp illumination (simulated solar light) the plasmonic enhancement of the Au NPs counterbalances the loss of photocurrent in the UV light range (ascribed to trapping effects; see section 3.3).

Interestingly, the net photocurrent difference ($\Delta I_{ph, +1000mV}$) between Au-TiO₂ and pristine TiO₂ photo-anodes measured under full lamp illumination is 3.6 $\mu\text{A cm}^{-2}$, which is remarkably smaller than the photocurrent measured for Au-TiO₂ photo-anodes with the 420 nm cutoff filter,

i.e. $8.0 \mu\text{A cm}^{-2}$. This is also evident when comparing data in Fig. 3d with the photocurrent transients in Fig. S8a – measured at +500 mV vs. Ag/AgCl under AM 1.5 illumination with 420 nm cutoff filter. In addition, the photocurrent transients in Fig. S8b, measured under chopped illumination provided by a 520 nm laser, further validate the plasmonic contribution and the stability of the plasmonic effect. More importantly, the reason for such a discrepancy can be that under combined UV and visible light illumination, the extraction of hot electrons from Au can be less favorable as the concurrent promotion of TiO₂ CB electrons under UV light illumination leads to an upward shift of the semiconductor Fermi level, which in turn increases the height of the Au-TiO₂ Schottky junction, thus reducing to some extent the hot electron injection efficiency. The visible light photocurrent ($\lambda > 420 \text{ nm}$) generated by the Au-TiO₂ structure is $8.0 \mu\text{A cm}^{-2}$ at +1000 mV, which is more than 10 times higher than that reported in the literature for comparable architectures,⁴³ and is even 8 times higher than that of thicker TiO₂ photo-anodes tested under higher applied potentials.¹⁶

Finally, to rule out the possibility that the observed visible light photocurrent may originate from artefacts, e.g. from the Si substrates, we produced TiO₂ surfaces identical to those described above, both pristine and decorated with dewetted Au NPs, on other (non-conductive) substrates such as Ti metal-coated SiO₂/Si wafers and quartz glass slides (see Scheme S1). The Au-decoration of these architectures was obtained by dewetting (450°C, 1 h, air) Au films with an initial thickness of 2 nm. The structures were tested as photo-anodes for PEC water splitting. The results (Fig. 3e,f) show that the Au-TiO₂ architectures generate visible light photocurrent even when formed on Ti/SiO₂/Si wafers and Ti/quartz glass slides.

4. Conclusions

In this work we fabricated Au nanoparticle-decorated TiO₂ surfaces for photo-electrochemical water splitting. Au nanoparticles were formed by solid state dewetting from sputtered thin Au films. Size and spacing of the nanoparticles could be controlled by adjusting the Au film initial

thickness. As a result, a fine tune of the Au NP size in the ~ 3 -200 nm range was enabled. The photo-electrochemical performance and optical features of the Au-TiO₂ surfaces were investigated in relation to the Au NP size and decoration density, considering parameters such as free TiO₂ surface, shading effects, hot carrier generation and extraction efficiency, and electron trapping effects. All Au-decorated photo-anodes enabled solar photo-electrochemical water splitting, showing a plasmonic photocurrent in the visible range (450-750 nm). The photocurrent response was the highest for ~ 30 nm-sized Au nanoparticles. As expected, optical absorption measurements show a red shift of the plasmonic extinction with increasing the Au NP size. However, the plasmonic photocurrent peaked at ~ 600 nm regardless of the Au particle size. Such a discrepancy is caused by a hot electron injection cut off effect that sets-in in a photo-electrochemical configuration due to the wavelength-dependence nature of the plasmonic decay. Moreover, the Au-TiO₂ surfaces showed a 16% higher solar PEC water splitting performance compared to pristine TiO₂ surfaces, and the plasmonic response measured under the sole visible light illumination was found to be significantly higher than that achieved under simultaneous with UV and visible light illumination. We propose that the UV semiconductor activation (band gap excitation) can limit the plasmonic hot electron injection from Au nanoparticles into TiO₂ due to an upward shift of the semiconductor Fermi level which in turns partially hinders the hot electron injection efficiency, owing to an increase of the Schottky barrier height.

Acknowledgements

The authors acknowledge the ERC, DFG, and DFG Cluster of Excellence EAM for financial support. The authors would like to acknowledge Ulrike Martens for the XRD analysis, Anja Friedrich for the SEM investigation, and Helga Hildebrand for the XPS measurements. Dr. Johannes Will (Chair of Micro- and Nanostructure Research, University of Erlangen-

Nuremberg, Erlangen, Germany) is also acknowledged for technical help with the XRD measurements.

References

- (1) Ni, M.; Leung, M. K.H.; Leung, D. Y.C.; Sumathy, K. A review and recent developments in photocatalytic water-splitting using TiO₂ for hydrogen production. *Renewable and Sustainable Energy Reviews* **2007**, *11*, 401–425.
- (2) Roy, P.; Berger, S.; Schmuki, P. TiO₂ nanotubes: Synthesis and applications. *Angew. Chem.* **2011**, *50*, 2904–2939.
- (3) Schneider, J.; Matsuoka, M.; Takeuchi, M.; Zhang, J.; Horiuchi, Y.; Anpo, M.; Bahnemann, D. W. Understanding TiO₂ photocatalysis: Mechanisms and materials. *Chemical reviews* **2014**, *114*, 9919–9986.
- (4) Robel, I.; Subramanian, V.; Kuno, M.; Kamat, P. V. Quantum dot solar cells. harvesting light energy with CdSe nanocrystals molecularly linked to mesoscopic TiO₂ films. *Journal of the American Chemical Society* **2006**, *128*, 2385–2393.
- (5) Zhu, K.; Neale, N. R.; Miedaner, A.; Frank, A. J. Enhanced charge-collection efficiencies and light scattering in dye-sensitized solar cells using oriented TiO₂ nanotubes arrays. *Nano Lett.* **2007**, *7*, 69–74.
- (6) Chen, H. M.; Chen, C. K.; Chang, Y.-C.; Tsai, C.-W.; Liu, R.-S.; Hu, S.-F.; Chang, W.-S.; Chen, K.-H. Quantum dot monolayer sensitized ZnO nanowire-array photoelectrodes: True efficiency for water splitting. *Angewandte Chemie (International ed.)* **2010**, *49*, 5966–5969.
- (7) Sun, W.-T.; Yu, Y.; Pan, H.-Y.; Gao, X.-F.; Chen, Q.; Peng, L.-M. CdS quantum dots sensitized TiO₂ nanotube-array photoelectrodes. *Journal of the American Chemical Society* **2008**, *130*, 1124–1125.
- (8) Zhang, J.; Jin, X.; Morales-Guzman, P. I.; Yu, X.; Liu, H.; Zhang, H.; Razzari, L.; Claverie, J. P. Engineering the Absorption and Field Enhancement Properties of Au-TiO₂ Nanohybrids via Whispering Gallery Mode Resonances for Photocatalytic Water Splitting. *ACS nano* **2016**, *10*, 4496–4503.
- (9) Zhang, Z.; Zhang, L.; Hedhili, M. N.; Zhang, H.; Wang, P. Plasmonic gold nanocrystals coupled with photonic crystal seamlessly on TiO₂ nanotube photoelectrodes for efficient visible light photoelectrochemical water splitting. *Nano letters* **2013**, *13*, 14–20.
- (10) Pu, Y.-C.; Wang, G.; Chang, K.-D.; Ling, Y.; Lin, Y.-K.; Fitzmorris, B. C.; Liu, C.-M.; Lu, X.; Tong, Y.; Zhang, J. Z. *et al.* Au nanostructure-decorated TiO₂ nanowires exhibiting photoactivity across entire UV-visible region for photoelectrochemical water splitting. *Nano letters* **2013**, *13*, 3817–3823.
- (11) Qian, K.; Sweeny, B. C.; Johnston-Peck, A. C.; Niu, W.; Graham, J. O.; DuChene, J. S.; Qiu, J.; Wang, Y.-C.; Engelhard, M. H.; Su, D. *et al.* Surface plasmon-driven water reduction: Gold nanoparticle size matters. *Journal of the American Chemical Society* **2014**, *136*, 9842–9845.
- (12) Gomathi Devi, L.; Kavitha, R. A review on plasmonic metal-TiO₂ composite for generation, trapping, storing and dynamic vectorial transfer of photogenerated electrons across the Schottky junction in a photocatalytic system. *Applied Surface Science* **2016**, *360*, 601–622.
- (13) Seh, Z. W.; Liu, S.; Low, M.; Zhang, S.-Y.; Liu, Z.; Mlayah, A.; Han, M.-Y. Janus Au-TiO₂ photocatalysts with strong localization of plasmonic near-fields for efficient visible-light hydrogen generation. *Advanced materials* **2012**, *24*, 2310–2314.
- (14) Li, Z.; Shi, L.; Franklin, D.; Koul, S.; Kushima, A.; Yang, Y. Drastic enhancement of photoelectrochemical water splitting performance over plasmonic Al@TiO₂ heterostructured nanocavity arrays. *Nano Energy* **2018**, *51*, 400–407.
- (15) Hou, W.; Cronin, S. B. A Review of Surface Plasmon Resonance-Enhanced Photocatalysis. *Adv. Funct. Mater.* **2013**, *23*, 1612–1619.

- (16) DuChene, J. S.; Sweeny, B. C.; Johnston-Peck, A. C.; Su, D.; Stach, E. A.; Wei, W. D. Prolonged hot electron dynamics in plasmonic-metal/semiconductor heterostructures with implications for solar photocatalysis. *Angewandte Chemie (International ed.)* **2014**, *53*, 7887–7891.
- (17) Bian, Z.; Tachikawa, T.; Zhang, P.; Fujitsuka, M.; Majima, T. Au/TiO₂ superstructure-based plasmonic photocatalysts exhibiting efficient charge separation and unprecedented activity. *Journal of the American Chemical Society* **2014**, *136*, 458–465.
- (18) Lee, J.; Mubeen, S.; Ji, X.; Stucky, G. D.; Moskovits, M. Plasmonic photoanodes for solar water splitting with visible light. *Nano letters* **2012**, *12*, 5014–5019.
- (19) Linic, S.; Christopher, P.; Ingram, D. B. Plasmonic-metal nanostructures for efficient conversion of solar to chemical energy. *Nature materials* **2011**, *10*, 911–921.
- (20) Nishijima, Y.; Ueno, K.; Yokota, Y.; Murakoshi, K.; Misawa, H. Plasmon-Assisted Photocurrent Generation from Visible to Near-Infrared Wavelength Using a Au-Nanorods/TiO₂ Electrode. *J. Phys. Chem. Lett.* **2010**, *1*, 2031–2036.
- (21) Torrell, M.; Kabir, R.; Cunha, L.; Vasilevskiy, M. I.; Vaz, F.; Cavaleiro, A.; Alves, E.; Barradas, N. P. Tuning of the surface plasmon resonance in TiO₂/Au thin films grown by magnetron sputtering: The effect of thermal annealing. *Journal of Applied Physics* **2011**, *109*, 74310.
- (22) Yan, J.; Wu, G.; Guan, N.; Li, L.; Li, Z.; Cao, X. Understanding the effect of surface/bulk defects on the photocatalytic activity of TiO₂: Anatase versus rutile. *Physical chemistry chemical physics* **2013**, *15*, 10978–10988.
- (23) Sham, T. K.; Lazarus, M. S. X-ray photoelectron spectroscopy (XPS) studies of clean and hydrated TiO₂ (rutile) surfaces. *Chemical Physics Letters* **1979**, *68*, 426–432.
- (24) Thompson, C. V. Solid-State Dewetting of Thin Films. *Annu. Rev. Mater. Res.* **2012**, *42*, 399–434.
- (25) Leroy, F.; Borowik, Ł.; Cheynis, F.; Almadori, Y.; Curiotto, S.; Trautmann, M.; Barbé, J. C.; Müller, P. How to control solid state dewetting: A short review. *Surface Science Reports* **2016**, *71*, 391–409.
- (26) Altomare, M.; Nguyen, N. T.; Schmuki, P. Templated dewetting: Designing entirely self-organized platforms for photocatalysis. *Chemical science* **2016**, *7*, 6865–6886.
- (27) Yoo, J. E.; Lee, K.; Altomare, M.; Selli, E.; Schmuki, P. Self-Organized Arrays of Single-Metal Catalyst Particles in TiO₂ Cavities: A Highly Efficient Photocatalytic System. *Angew. Chem.* **2013**, *125*, 7662–7665.
- (28) Spanu, D.; Recchia, S.; Mohajernia, S.; Tomanec, O.; Kment, Š.; Zboril, R.; Schmuki, P.; Altomare, M. Templated Dewetting–Alloying of NiCu Bilayers on TiO₂ Nanotubes Enables Efficient Noble-Metal-Free Photocatalytic H₂ Evolution. *ACS Catal.* **2018**, *8*, 5298–5305.
- (29) Nguyen, N. T.; Altomare, M.; Yoo, J. E.; Taccardi, N.; Schmuki, P. Noble Metals on Anodic TiO₂ Nanotube Mouths: Thermal Dewetting of Minimal Pt Co-Catalyst Loading Leads to Significantly Enhanced Photocatalytic H₂ Generation. *Adv. Energy Mater.* **2016**, *6*, 1501926.
- (30) Henderson, M. A. A surface science perspective on TiO₂ photocatalysis. *Surface Science Reports* **2011**, *66*, 185–297.
- (31) Nguyen, N. T.; Altomare, M.; Yoo, J.; Schmuki, P. Efficient Photocatalytic H₂ Evolution: Controlled Dewetting-Dealloying to Fabricate Site-Selective High-Activity Nanoporous Au Particles on Highly Ordered TiO₂ Nanotube Arrays. *Advanced materials* **2015**, *27*, 3208–3215.
- (32) Spanu, D.; Recchia, S.; Mohajernia, S.; Schmuki, P.; Altomare, M. Site-selective Pt dewetting on WO₃-coated TiO₂ nanotube arrays: An electron transfer cascade-based H₂ evolution photocatalyst. *Applied Catalysis B: Environmental* **2018**, *237*, 198–205.

- (33) Altomare, M.; Nguyen, N. T.; Hejazi, S.; Schmuki, P. A Cocatalytic Electron-Transfer Cascade Site-Selectively Placed on TiO₂ Nanotubes Yields Enhanced Photocatalytic H₂ Evolution. *Adv. Funct. Mater.* **2018**, *28*, 1704259.
- (34) Kimura, K.; Naya, S.-i.; Jin-nouchi, Y.; Tada, H. TiO₂ Crystal Form-Dependence of the Au/TiO₂ Plasmon Photocatalyst's Activity. *J. Phys. Chem. C* **2012**, *116*, 7111–7117.
- (35) Wang, H.; You, T.; Shi, W.; Li, J.; Guo, L. Au/TiO₂/Au as a Plasmonic Coupling Photocatalyst. *J. Phys. Chem. C* **2012**, *116*, 6490–6494.
- (36) Yoo, S. M.; Rawal, S. B.; Lee, J. E.; Kim, J.; Ryu, H.-Y.; Park, D.-W.; Lee, W. I. Size-dependence of plasmonic Au nanoparticles in photocatalytic behavior of Au/TiO₂ and Au@SiO₂/TiO₂. *Applied Catalysis A: General* **2015**, *499*, 47–54.
- (37) Peerakiatkhajohn, P.; Butburee, T.; Yun, J.-H.; Chen, H.; Richards, R. M.; Wang, L. A hybrid photoelectrode with plasmonic Au@TiO₂ nanoparticles for enhanced photoelectrochemical water splitting. *J. Mater. Chem. A* **2015**, *3*, 20127–20133.
- (38) Wen, Y.; Liu, B.; Zeng, W.; Wang, Y. Plasmonic photocatalysis properties of Au nanoparticles precipitated anatase/rutile mixed TiO₂ nanotubes. *Nanoscale* **2013**, *5*, 9739–9746.
- (39) Ginsburg, A.; Priel, M.; Barad, H. N.; Keller, D. A.; Borvick, E.; Rietwyk, K.; Kama, A.; Meir, S.; Anderson, A. Y.; Zaban, A. Solid state ITO|Au-NPs|TiO₂ plasmonic based solar cells. *Solar Energy Materials and Solar Cells* **2018**, *179*, 254–259.
- (40) Minutella, E.; Schulz, F.; Lange, H. Excitation-Dependence of Plasmon-Induced Hot Electrons in Gold Nanoparticles. *The journal of physical chemistry letters* **2017**, *8*, 4925–4929.
- (41) Valenti, M.; Jonsson, M. P.; Biskos, G.; Schmidt-Ott, A.; Smith, W. A. Plasmonic nanoparticle-semiconductor composites for efficient solar water splitting. *J. Mater. Chem. A* **2016**, *4*, 17891–17912.
- (42) Wu, N. Plasmonic metal-semiconductor photocatalysts and photoelectrochemical cells: A review. *Nanoscale* **2018**, *10*, 2679–2696.
- (43) Zhan, Z.; An, J.; Zhang, H.; Hansen, R. V.; Zheng, L. Three-dimensional plasmonic photoanodes based on Au-embedded TiO₂ structures for enhanced visible-light water splitting. *ACS applied materials & interfaces* **2014**, *6*, 1139–1144.

Figure captions

Figure 1: A) Schematic and B-F) physicochemical characterization of TiO₂ surfaces (formed on Ti/Si wafers) decorated with dewetted Au nanoparticles. B) Cross-sectional SEM image of the sample after annealing (450°C, 1 h in air). C) X-ray diffraction pattern of as-sputtered and annealed (450°C, air, 1 h) architectures. D) XPS depth profile measurement of as-sputtered and annealed architectures. E) and F) AFM analysis of as-sputtered and annealed architectures (root mean squared (RMS) surface roughness results are reported as inset in E) and F)).

Figure 2: Top view SEM images of TiO₂ surfaces (formed on Ti/Si wafers) sputter-coated with Au films of various thicknesses: A) 0 nm, B) 0.5 nm, C) 1 nm, D) 2 nm, E) 3 nm, F) 5 nm, and G) 10 nm; all the structures were subjected to a thermal treatment in air at 450°C (1 h) to induce dewetting of the Au films into Au nanoparticles.

Figure 3: Photo-electrochemical (PEC) characterization of different Au NP-decorated TiO₂ surfaces (formed on Ti/Si wafers). A) IPCE spectra of TiO₂ surfaces coated with Au films of different thicknesses and then dewetted. B) Photocurrent density and IPCE values measured at 600 nm as a function of the Au film initial thickness. C) Photocurrent transients measured at 600 nm. D) Photoelectrochemical water-splitting behavior (linear sweep voltammetry) for pristine and Au NP-decorated TiO₂ surfaces measured under full lamp illumination and with 420 nm cut off filter. E) IPCE spectra of different pristine and Au NP-decorated TiO₂ surfaces formed on Ti/Si wafers, Ti/SiO₂/Si wafers and Ti-coated quartz slides. F) Magnified view (visible light range) of the IPCE spectra in E).

Figure 1

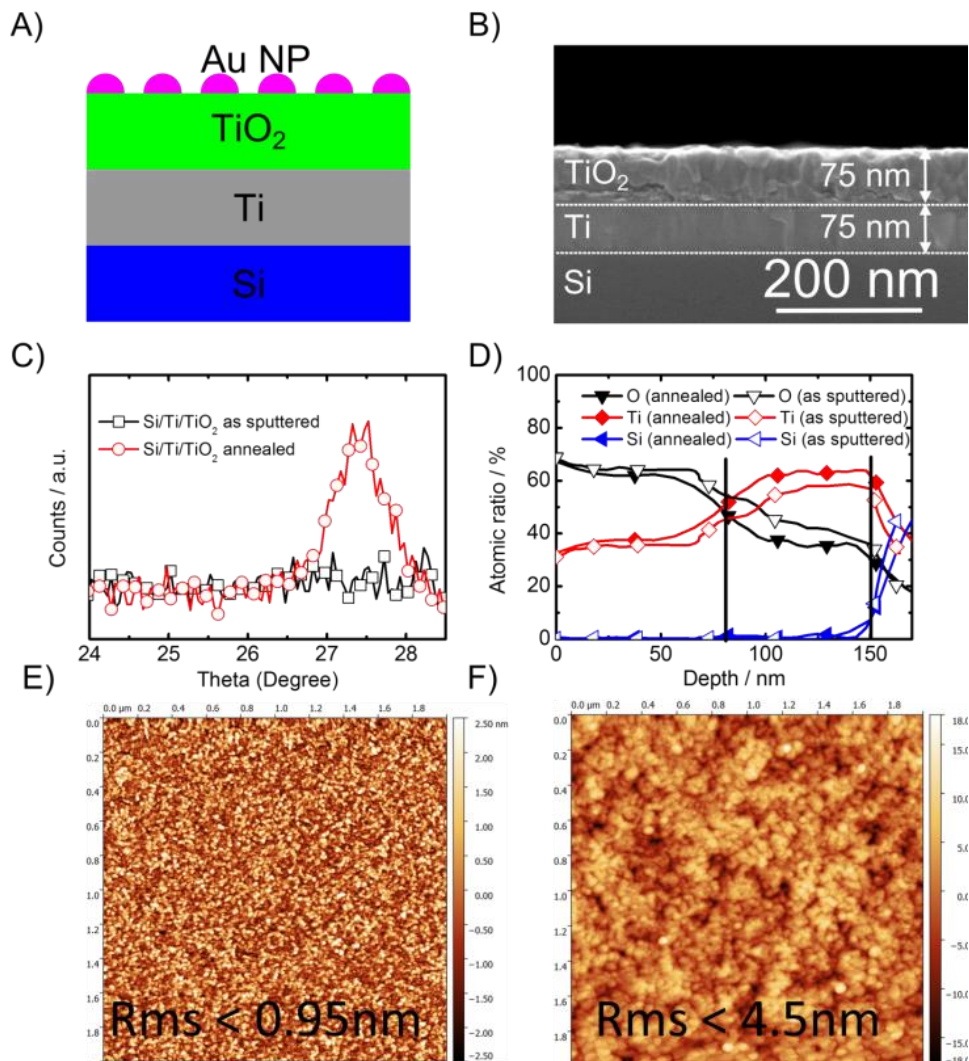


Figure 2

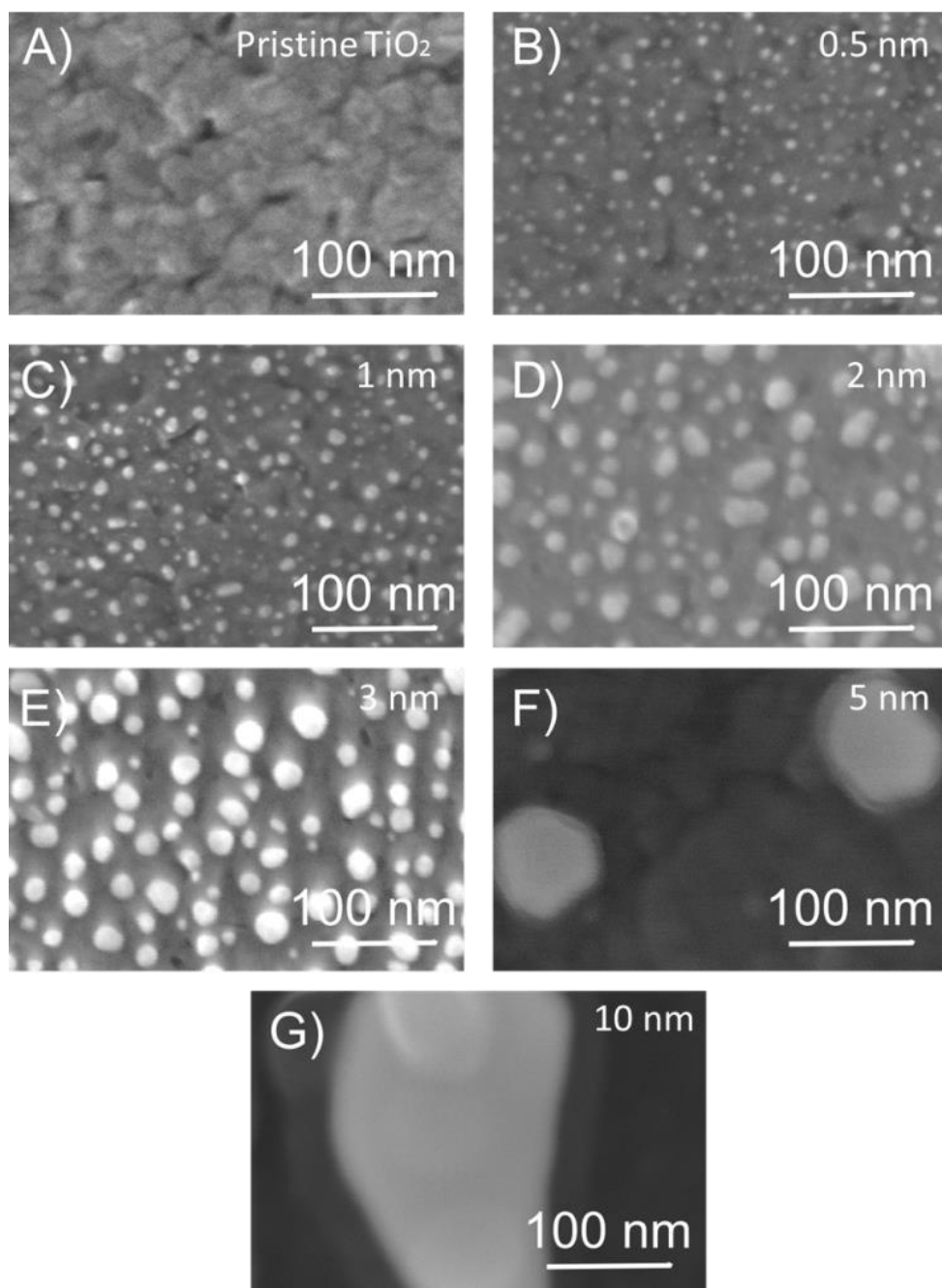


Figure 3

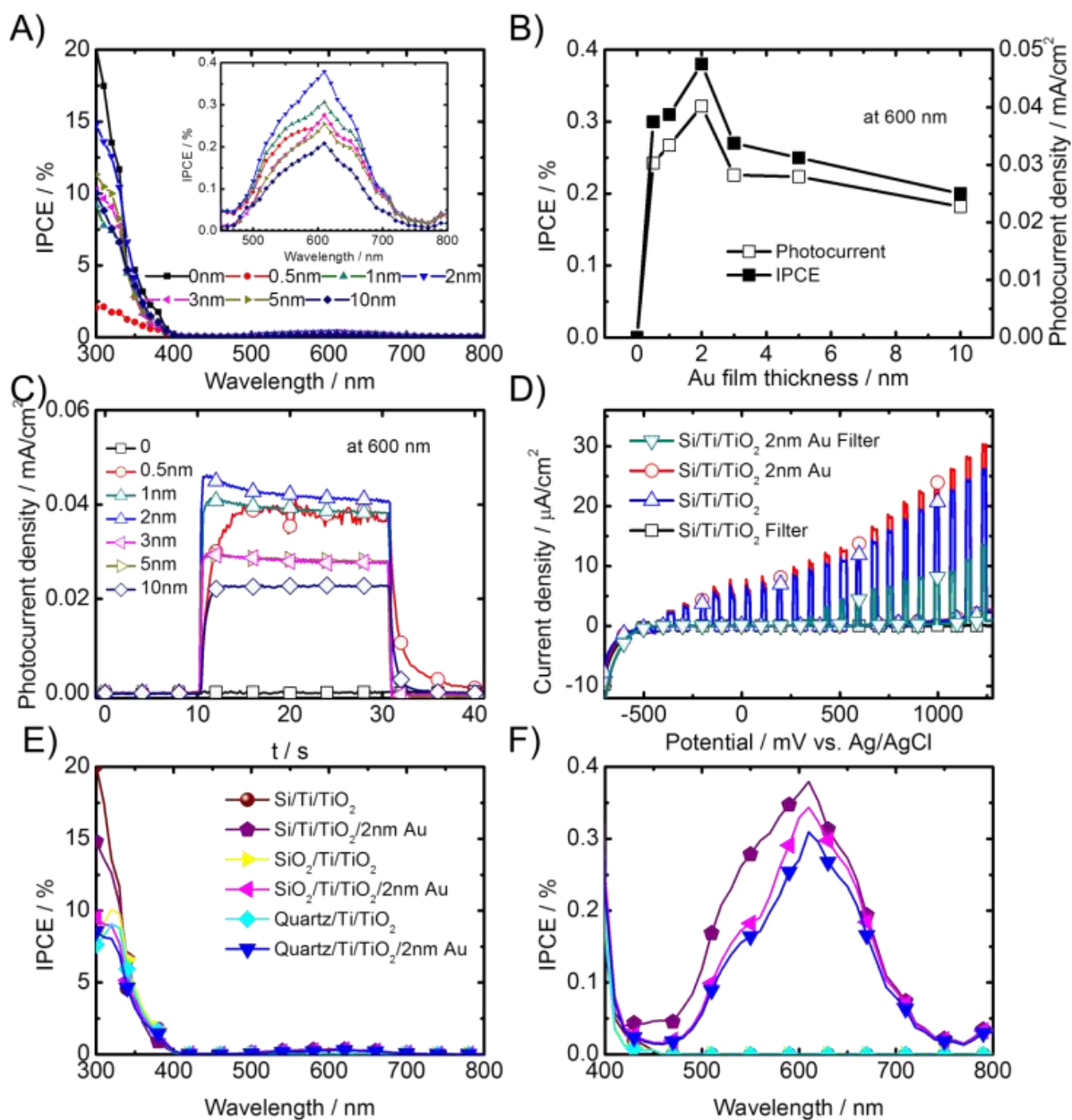


Table of contents (TOC)

